frontiers | Frontiers in Physics

TYPE Original Research
PUBLISHED 24 August 2022
DOI 10.3389/fphy.2022.961201

OPEN ACCESS

EDITED BY
Haibo Huang,
University of Science and Technology of China, China

REVIEWED BY
Maryiam Javed,
Institute of Space Technology, Pakistan
Safia Akram,
National University of Sciences and Technology, Pakistan
Noreen Sher Akbar,
National University of Sciences and Technology (NUST), Pakistan

*CORRESPONDENCE
Arshad Riaz,
arshad-riaz@ue.edu.pk

SPECIALTY SECTION
This article was submitted to Interdisciplinary Physics, a section of the journal Frontiers in Physics

RECEIVED 04 June 2022
ACCEPTED 27 June 2022
PUBLISHED 24 August 2022

CITATION
Riaz A, Ahammad NA, Alqarni MM, Hejazi HA and Tag-ElDin EM (2022), Peristaltic flow of a viscous fluid in a curved duct with a rectangular cross section.
Front. Phys. 10:961201.
doi: 10.3389/fphy.2022.961201

Peristaltic flow of a viscous fluid in a curved duct with a rectangular cross section

Arshad Riaz[1]*, N. Ameer Ahammad[2], M. M. Alqarni[3], Hala A. Hejazi[4] and ElSayed M. Tag-ElDin[5]

[1]Division of Science and Technology, Department of Mathematics, University of Education Lahore, Lahore, Pakistan, [2]Department of Mathematics, Faculty of Science, University of Tabuk, Tabuk, Saudi Arabia, [3]Department of Mathematics, College of Sciences, King Khalid University, Abha, Saudi Arabia, [4]Mathematical Sciences Department, College of Applied Sciences, Umm Al-Qura University, Makkah, Saudi Arabia, [5]Faculty of Engineering and Technology, Future University in Egypt, New Cairo, Egypt

Most flow systems in the human body are duct shaped, such as the pancreatic, bile, and gallbladder ducts. Such flow systems are also common in industrial applications like HVAC systems. This study presents a novel mathematical model to analyze the peristaltic motion of a viscous fluid in a three-dimensional curved duct with a rectangular cross section; specifically, such geometries are used more in industrial and medical applications. In the current investigation, the constraints of lubrication theory are considered, and a perturbation technique is used to solve the Navier–Stokes partial differential equations. The major focus of this work is on the aspect ratio of the duct and curvature of the flow axis. Curvilinear coordinates of cylindrical systems are considered for the derivations because of the curved geometry; homogeneous no-slip boundary conditions are proposed at the flexible surfaces, and the expression for pressure increase is found numerically using the NIntegrate tool of computing software Mathematica. A comprehensive graphical discussion is presented to determine the effects of all salient physical factors related to the problem. The results show that the large curvature and aspect ratio reduce the fluid speed gradually but that the flow rate promotes fluid velocity. The pumping rate is a decreasing function of the curvature and aspect ratio; however, reverse pumping can occur for large curvature values. Streamline evaluations suggest that large wave amplitudes increase the number of circulating boluses.

KEYWORDS

curved duct, peristaltic flow, homogeneous conditions, Newtonian (viscous) fluid, perturbation method, curvilinear/cylindrical coordinates

Introduction

Peristalsis refers to a flow pattern in which a fluid is transported by a sequence of waves generated by the expansion and compression of the walls of a conduit. This phenomenon occurs in many of the human organs, including movement of food in the esophagus, blood circulation in the arteries from pumping by the heart, and urine transportation from the kidney to bladder. This phenomenon can also be seen in other

living organisms such as leeches, which have the ability to suck blood and push it through their bodies by peristaltic pumping patterns, because of which they are commonly used in the treatment of tumors, mental diseases, and skin diseases by removing blood from the affected parts of the body. Peristaltic flow mechanisms are also applicable to industrial scenarios, such as the transportation of sanitary fluids, toxic liquid flows in nuclear production, and transport of corrosive fluids. This approach is also used in most medical equipment, such as blood pumps and heart-lung machines. Shapiro et al. [1] explained the basic principles and highlighted the importance of the various physical parameters of the flow mechanism. Surveys of critical research and hypotheses on the peristaltic flow mechanisms of multiple flow models have been widely discussed and presented in open literature based on the assumptions of large wavelengths and low Reynolds numbers.

Many scientific researchers and biologists are working on this topic owing to its wide usage in several industrial processes as well as clinical phenomena. Researchers have incorporated various types of geometries into their studies like symmetric/asymmetric channels, tubes, endoscopes, curved channels, and straight/rectangular/square ducts. The main focus of this work is on recent studies in the field. Kumari and Radhakrishnamacharya [2] presented peristaltic flow in an inclined channel with slip and magnetic effects; they observed that the mean flow speed increases with the slip factor but decreases because of the magnetic field and porosity of the space. Mekheimer [3] investigated blood flow in a nonuniform channel under the effect of a magnetic field and calculated that the peristaltic pressure is a direct function of the magnetic field. Rashid et al. [4] reported peristaltic flow in a curved channel for the Williamson model and suggested that the model induces a large increase in pressure compared to that of a viscous liquid. Haroun [5] reported the peristaltic flow of a fourth-grade fluid in an inclined asymmetric channel and noted that the trapping region enlarges as the channel becomes symmetric; further, the pressure increase is maximum for a non-Newtonian fluid than a Newtonian one. Javed and Naz [6] considered the Jeffrey fluid for pumping flow in an asymmetric channel and observed that reverse pumping occurs near the channel walls. Other relevant studies on viscous fluid flows in channels have also been reported [7–17].

The abovementioned studies considered mostly symmetric or asymmetric straight channels. However, owing to the wide range of applications of curved geometries in many physiological flow regions, some researchers have considered curved channels in their work and provided vital contributions. Hina et al. [18] considered a compliant curved channel to study peristaltic flow using the Johnson–Segalman model through the thermal and mass transfer effects; their study shows that a large temperature distribution can be obtained in a curved channel compared to the straight one, but the heat coefficient is minimum in the curved channel. Nadeem and Shahzadi [19] studied two-phase nanofluid flow in a curved channel and noted that the large curvature of the conduit increases the peristaltic pressure; they also observed that the temperature distribution was large owing to the large curvature. Kalantri et al. [20] numerically investigated non-Newtonian peristaltic transport across a curved channel and noted that an increase in the elastic characteristics of the non-Newtonian fluid causes a decrease in the pumping pressure. Tanveer et al. [21] investigated mixed convection in the peristaltic flow of the Eyring–Powell model in a curved channel and observed that the velocity increased greatly by the large Brownian diffusion but reduced for larger thermophoresis. Thus, an increase in thermal exchange has been reported in the case of increasing curvature. Nadeem and Maraj [22] evaluated the peristaltic stream of the hyperbolic tangent fluid model in a curved container; they observed that the left-sided velocity decreases with the curvature factor but the right-sided velocity increases with the same factor. It is further noted that the pressure increase is inversely dependent upon the curvature parameter; more studies on pumping flows in curved channels are reported in [23–28].

Most real-life peristaltic flows are three dimensional in nature and occur in ducts with rectangular or square cross sections. Only a few researchers have considered three-dimensional conduits for transportation and duct motion of Newtonian and non-Newtonian fluids in rectangular ducts. Reddy et al. [29] investigated duct peristaltic flow and reported the wall properties of the duct. The main focus of the present study is elucidating the effects of aspect ratio of the wall dimensions on various flow parameters. The pressure increase and flow rates were measured for different values of the aspect ratio, and it was concluded that the pressure rise is a decreasing function of the aspect ratio. Nadeem and Akram [30] investigated the Jeffrey fluid flow in a rectangular duct and reported that the axial pressure increases with increasing aspect ratios; the authors also compared their findings with the results of channel and square duct flows by considering some special cases and concluded that the peristaltic pressure is higher in a rectangular duct than a two-dimensional channel or square duct. Riaz [31] recently reported the thermal and mass exchange effects on the peristaltic flow of the Eyring–Powell fluid in a rectangular duct and suggested that the rates of heat and mass transfer are less for the considered model than a Newtonian fluid but can be enhanced by increasing the aspect ratio. Abbas et al. [32] used a nonuniform rectangular duct with elastic walls to examine the wave transport of the hyperbolic tangent fluid model and claimed that the fluid velocity increases with the aspect ratio of the conduit; they also claimed that the size of the trapped bolus decreases with non-Newtonian features. The above discussion indicates that peristaltic flow problems have been analyzed in channels (both straight and curved) but there are very few works available for ducts. Moreover, most industrial and medical equipment for pumping flows include curved three-dimensional ducts, but there are no reported studies on investigation of pumping flows in curved ducts. This is likely attributable to the complex modeling and simulation of the complicated partial differential equations (PDEs) representing such flows, which require large mathematical and

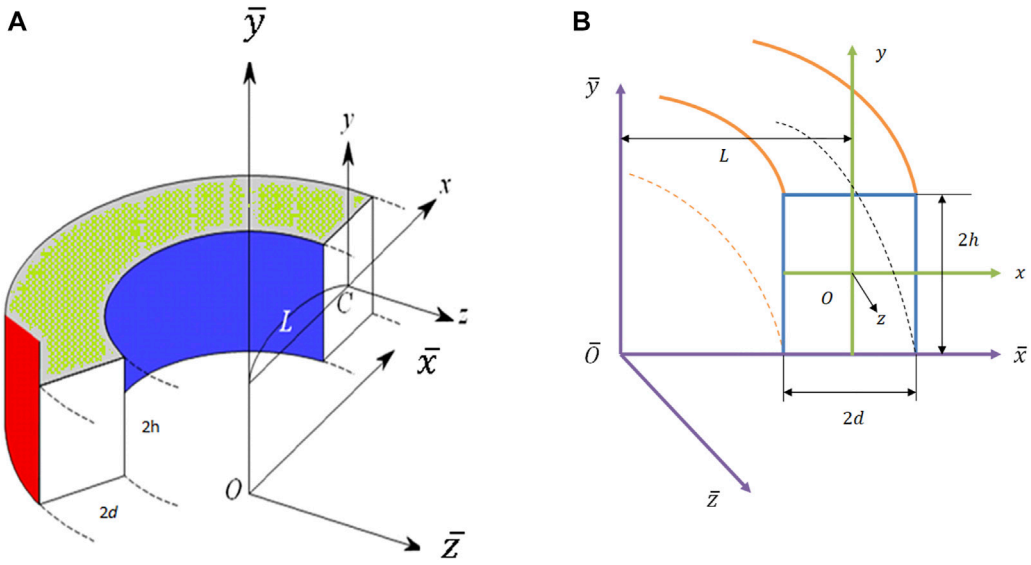

FIGURE 1
Geometrical view of a curved duct.

computer-assisted computations. In the present study, we examine such complicated work and derive some new results. The three-dimensional peristaltic flow is investigated in a curved duct with a rectangular cross section. The geometry of the problem is modeled using curvilinear coordinates through suitable transformations. An unsteady wavy flow is assumed with sinusoidal waves appearing on some walls with nonzero curvature. The cylindrical coordinate system is initially used for mathematical work that is later transformed to curvilinear coordinates in accordance with the geometrical structure. Some physical constraints are considered to simplify the calculations, such as a large wavelength and low Reynolds number approximations. The general mass and momentum conservation laws are considered and derived using dimensionless variables in the transformations. No-slip boundary conditions are assumed to derive the particular solutions; the expression for velocity is determined analytically, and the pressure rise is obtained numerically using the computational software Mathematica.

Mathematical modeling

Let us assume a Newtonian fluid flow in a three-dimensional curved duct with a rectangular cross section of height $2h$ and width $2d$ [33]. A peristaltic wave is propagated along the axial direction with a constant speed c. The orientation of the duct is assumed as follows: the peristaltic walls are along the vertical surfaces (y-axis) whose characteristics are functions of angle θ and time t; L is the reference length from the central point O, as shown in Figure 1. The flow geometry is considered in the cylindrical coordinate system, so r, θ, and y are assumed as the coordinates.

The flow in a curved rectangular duct is represented by the following mathematical forms of the physical laws, i.e., conservation of mass and momentum, as [33]

$$rD_r(u) + D_\theta(w) + rD_y(v) + u = 0 \tag{1}$$

$$\rho r\left(D_t(u) + (A\cdot\mathrm{del})u\right) - \rho v^2 = -rD_r(p) + \mu r^{-1}\left(r^2\Delta^* u - u - 2D_\theta(v)\right), \tag{2}$$

$$\rho r\left(D_t(w) + (A\cdot\mathrm{del})w\right) + \rho uw = -D_\theta(p) + \mu r^{-1}\left(r^2\Delta^* w - w + 2D_\theta(u)\right), \tag{3}$$

$$\rho\left(D_t(v) + (A\cdot\mathrm{del})v\right) = -D_y(p) + \mu(\Delta^* v). \tag{4}$$

Here, $D_j\ for\ (j = t, r, \theta, z)$; $A\cdot\mathrm{del}$ and Δ^* are the first and second order differential operators defined as follows:

$$A\cdot\mathrm{del} = uD_r + wr^{-1}D_\theta + vD_y,\ \Delta^* = D_{rr} + r^{-1}D_r + r^{-2}D_{\theta\theta} + D_{yy}$$

The wave generating wall function (curved) is described as [27, 28]

$$\tilde{a}(\theta, t) = h + b\cos\frac{2\pi}{\lambda}\left(X' - ct\right),\ where\ X' = L\theta, \tag{5}$$

where b is the wave amplitude, and λ is the wavelength. The following transformations are considered for the purpose of nondimensionlization of the above expressions:

$$\lambda\bar{t} - ct = 0,\ c\xi\bar{u} - u = 0,\ c\xi\bar{v} - v = 0,\ c\bar{w} - w = 0,\ r - (L + d\bar{x}) = 0,\ y - h\bar{y} = 0, X' - \lambda\bar{z} = 0,\ c\lambda\mu\bar{p} - d^2 p = 0,\ h\bar{a} = \tilde{a} \tag{6}$$

Here, ξ $(= \frac{h}{\lambda})$ is the wavenumber, μ is the fluid viscosity, t is the time, and p is the pressure. Thus, the expressions defined in Eqs. 1–6 can be transformed to the subsequent form as follows:

$$\alpha\frac{\partial\bar{u}}{\partial\bar{x}} + \frac{1}{1+\delta\bar{x}}\frac{\partial\bar{w}}{\partial\bar{z}} + \frac{\partial\bar{v}}{\partial\bar{y}} + \frac{\alpha\delta}{1+\delta\bar{x}}\bar{u} = 0 \tag{7}$$

$$Re\,\xi\left(\xi^2\frac{\partial\bar{u}}{\partial\bar{t}} + \alpha\xi^2\bar{u}\frac{\partial\bar{u}}{\partial\bar{x}} + \xi^2\bar{v}\frac{\partial\bar{u}}{\partial\bar{y}} + \frac{\xi\bar{w}}{1+\delta\bar{x}}\frac{\partial\bar{u}}{\partial\bar{z}} - \frac{\alpha\delta}{1+\delta\bar{x}}\bar{w}^2\right) = \alpha^3\xi^2\left(\alpha^2\frac{\partial^2\bar{u}}{\partial\bar{x}^2} + \frac{\delta\alpha^2}{1+\delta\bar{x}}\frac{\partial\bar{u}}{\partial\bar{x}} + \frac{\xi^2\bar{w}}{(1+\delta\bar{x})^2}\frac{\partial^2\bar{u}}{\partial\bar{z}^2} + \frac{\partial^2\bar{u}}{\partial\bar{y}^2} - \left(\frac{\alpha\delta}{1+\delta\bar{x}}\right)^2\bar{u} - \alpha\left(\frac{4\delta^{1/2}}{1+\delta\bar{x}}\right)^2\frac{\partial\bar{w}}{\partial\bar{z}}\right) - \alpha^2\frac{\partial\bar{p}}{\partial\bar{x}}, \tag{8}$$

$$Re\,\xi\left(\alpha\frac{\partial\bar{w}}{\partial\bar{t}} + \alpha^2\bar{u}\frac{\partial\bar{w}}{\partial\bar{x}} + \alpha\bar{v}\frac{\partial\bar{w}}{\partial\bar{y}} + \frac{\alpha\bar{w}}{(1+\delta\bar{x})}\frac{\partial\bar{w}}{\partial\bar{z}} + \frac{\alpha\delta}{(1+\delta\bar{x})}\bar{u}\bar{w}\right) = \left(\alpha^2\frac{\partial^2\bar{w}}{\partial\bar{x}^2} + \frac{\delta\alpha^2}{1+\delta\bar{x}}\frac{\partial\bar{w}}{\partial\bar{x}} + \frac{\xi^2}{(1+\delta\bar{x})^2}\frac{\partial^2\bar{w}}{\partial\bar{z}^2} + \frac{\partial^2\bar{w}}{\partial\bar{y}^2} - \left(\frac{\alpha\delta}{1+\delta\bar{x}}\right)^2\bar{w} + \alpha\xi^2\left(\frac{4\delta^{1/2}}{1+\delta\bar{x}}\right)^2\frac{\partial\bar{u}}{\partial\bar{z}}\right) - \frac{\alpha^2}{1+\delta\bar{x}}\frac{\partial\bar{p}}{\partial\bar{z}}, \tag{9}$$

$$Re\,\xi^3\left(\frac{1}{\alpha}\frac{\partial\bar{w}}{\partial\bar{t}} + \bar{u}\frac{\partial\bar{v}}{\partial\bar{x}} + \frac{1}{\alpha}\bar{v}\frac{\partial\bar{v}}{\partial\bar{y}} + \frac{\bar{w}}{\alpha(1+\delta\bar{x})}\frac{\partial\bar{v}}{\partial\bar{z}}\right) = \xi^2\left(\frac{\partial^2\bar{v}}{\partial\bar{x}^2} + \frac{\delta}{1+\delta\bar{x}}\frac{\partial\bar{v}}{\partial\bar{x}} + \frac{\xi^2}{\alpha^2(1+\delta\bar{x})^2}\frac{\partial^2\bar{v}}{\partial\bar{z}^2} + \frac{1}{\alpha^2}\frac{\partial^2\bar{v}}{\partial\bar{y}^2}\right) - \frac{\partial\bar{p}}{\partial\bar{y}}. \tag{10}$$

For the above equations, the generated dimensionless parameters are as follows:

$$\alpha = \frac{h}{d},\ \delta = \frac{d}{L},\ Re = \frac{\rho dc}{\mu},\ \xi = \frac{h}{\lambda},\ \phi = \frac{b}{h}. \tag{11}$$

Using the criteria of large wavelength and low Reynolds number, the simplified versions of Eqs. 8–10 are obtained as follows (except for the bar symbols):

$$\frac{\alpha^2}{1+\delta x}\frac{dp}{dz} = \alpha^2\frac{\partial^2 w}{\partial x^2} + \frac{\delta\alpha^2}{1+\delta x}\frac{\partial w}{\partial x} + \frac{\partial^2 w}{\partial y^2} - \left(\frac{\alpha\delta}{1+\delta x}\right)^2 w. \tag{12}$$

The corresponding boundary conditions of the flow problem are given by [31]

$$w\left(\bar{x}, \pm\tilde{a}\right) = 0 \text{ and } w\left(\pm d, \bar{y}\right) = 0 \tag{13}$$

In the dimensionless form, Eq. 13 has no bar signs and is given by

$$w(x, \pm a) = 0 \text{ and } w\left(\pm 1, y\right) = 0, \text{where } a = 1 + \phi\cos 2\pi(z - t) \tag{14}$$

Solution scheme

To solve the linear partial differential equation in Eq. 12 using the boundary conditions in Eqs. 13, 14, the well-known homotopy perturbation method (HPM) is used [34–36]. The linear operator assumed in the process is $\chi_{yy} = \partial^2/\partial y^2$. The initial estimate satisfying the conditions is given as $w_0 = \frac{\frac{dp}{dz}(-a^2+y^2)\alpha^2}{2+2x\delta}$. The zeroth and first order systems have the following respective forms:

$$\chi_{yy}\hat{w}_0 - \chi_{yy}w_0 = 0,\ \hat{w}_0(x, \pm a) = 0 \text{ and } \hat{w}_0\left(\pm 1, y\right) = 0 \tag{15}$$

$$\chi_{yy}\hat{w}_1 + \chi_{yy}\hat{w}_0 + \alpha^2\chi_{xx}\hat{w}_0 + \frac{\delta\alpha^2}{1+\delta x}\chi_x\hat{w}_0 - \left(\frac{\alpha\delta}{1+\delta x}\right)^2 w - \frac{\alpha^2}{1+\delta x}\,dp\Big/dz = 0,\ \hat{w}_1(x, \pm a) = 0 \text{ and } \hat{w}_1\left(\pm 1, y\right) = 0. \tag{16}$$

By solving these two systems simultaneously on Mathematica using the DSolve command, we obtained the final solution of the axial velocity w as follows:

$$w(x, y) = -\frac{1}{80(1+x\delta)^5}\left(dp/dz\,(a-y)(a+y)\alpha^2(40 + 160x\delta + 240x^2\delta^2 160x^3\delta^3 + (40x^4 + (61a^4 - 14a^2y^2 + y^4)\alpha^4)\delta^4)\right). \tag{17}$$

The flow rate in the dimensional form is given by

$$\bar{F} = \int_{-d}^{d}\int_{-\tilde{a}}^{\tilde{a}} w dr dy. \tag{18}$$

In the dimensionless format, $(\bar{F} = dhcQ)$ and reduces to (after removing the bars)

$$Q = \int_{-1}^{1}\int_{-a}^{a} w dx dy \tag{19}$$

By solving Eqs. 18, 19 for dp/dz, we obtain

$$\frac{dp}{dz} = -\frac{Q}{\frac{68\,a^7\,\alpha^6\,\delta^4\,(1+\delta^2)}{35\,(-1+\delta^2)^4} + \frac{4a^3\alpha^2\tanh^{-1}\delta}{3\delta}} \tag{20}$$

The pressure increase is implemented numerically in Mathematica using the following expression:

$$\Delta p = \int_0^1\left(\frac{dp}{dz}\right)dz. \tag{21}$$

Graphical results and discussion

In this section, some of the physical quantities noted previously are examined through graphs of the axial velocity versus curvature, axial pressure slope, pressure rise, and trapped bolus to observe the

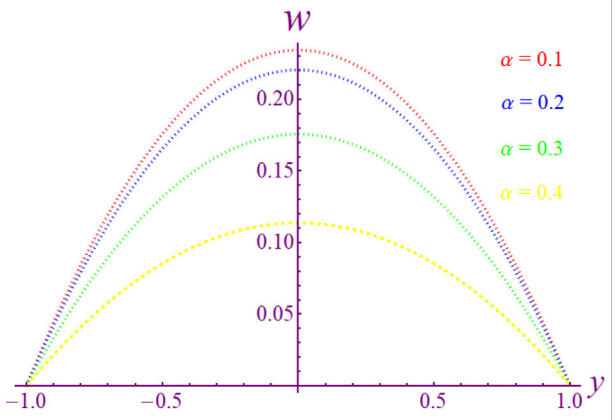

FIGURE 2
Axial velocity variation with respect to aspect ratio α.

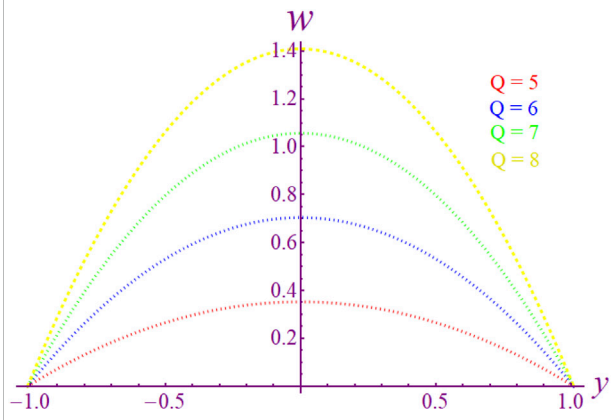

FIGURE 4
Axial velocity variation with respect to flow rate Q.

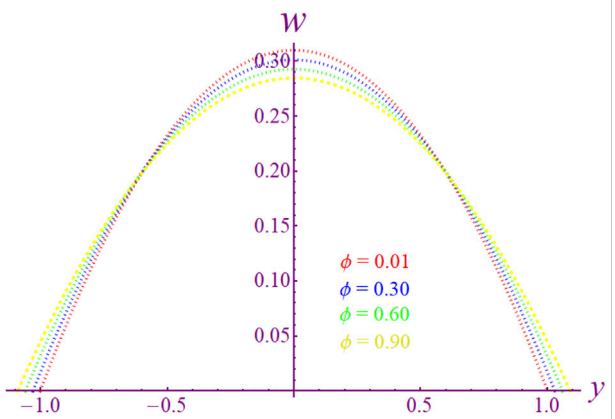

FIGURE 3
Axial velocity variation with respect to amplitude ratio ϕ.

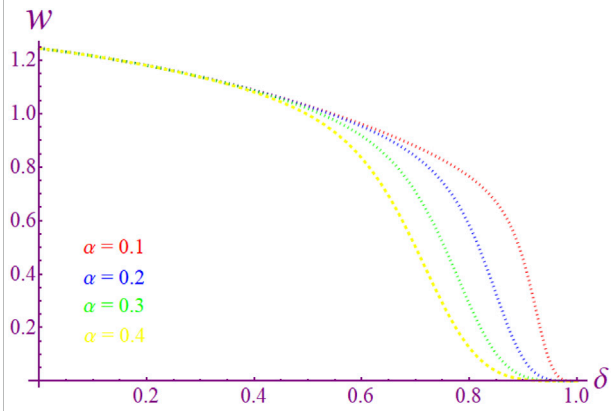

FIGURE 5
w-δ curves for α.

behavior of the flow properties. In Figures 2–4, the axial velocity is plotted against input y for increases in the absolute values of the aspect ratio (α), amplitude ratio ϕ, and flow rate Q. These graphs are structured such that the range of coordinate y is $[-a, a]$, where a is the wave height function that is directly related to the axial coordinate z and time t. To understand the velocity variations for domains with varying curvatures, Figures 5–7 are plotted showing the impacts of α, ϕ, and Q on the velocity profile w, respectively. These graphs represent the overall impact of the duct curvature on the fluid velocity for various parameters. In these diagrams, a uniform range $\delta \in [0, 1]$ is considered to investigate the curvature impact on flow. Figures 8–10 show the quantitative analysis estimates of the axial pressure variation dp/dz against axial coordinate z for parameters α, δ, and Q, respectively. Figures 11–13 predict the peristaltic pumping rates Δp along the flow rate Q to determine the effects of α, δ, and ϕ separately. The trapped bolus phenomenon is depicted in Figures 14, 15 to examine the flow patterns under factors α, δ, and ϕ, respectively. These figures show uniformly circulating closed contours that predict the contraction and expansion of the flexible tissues comprising the duct walls and also show the pumping scenario diagrammatically.

Figure 2 graphically illustrates the axial velocity characteristics for increasing values of the aspect ratio α; it can be observed from the plot that the fluid velocity is directly affected by the aspect ratio, which is the ratio of the width to height of the rectangular cross section of the duct, such that the increasing aspect ratio indicates increasing length when the height is fixed. The aspect ratio exerts more pressure on the fluid so as to suppress the fluid flow intensity. It is also noted that the fluid speed is maximum at the center of the flow path and that there is static flow at the walls, proving that there is no slip along the surfaces of the duct. Figure 3 shows the velocity variation with amplitude ratio ϕ, and it is seen that a large amplitude ratio permits greater fluid intensity at the corners of the flow stream but has an opposite effect in the middle of the flow domain. This enables the justification for a large amplitude ratio in the

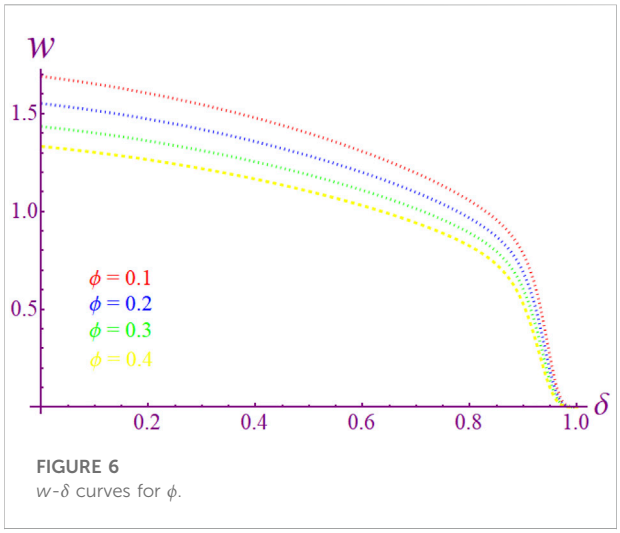

FIGURE 6
w-δ curves for ϕ.

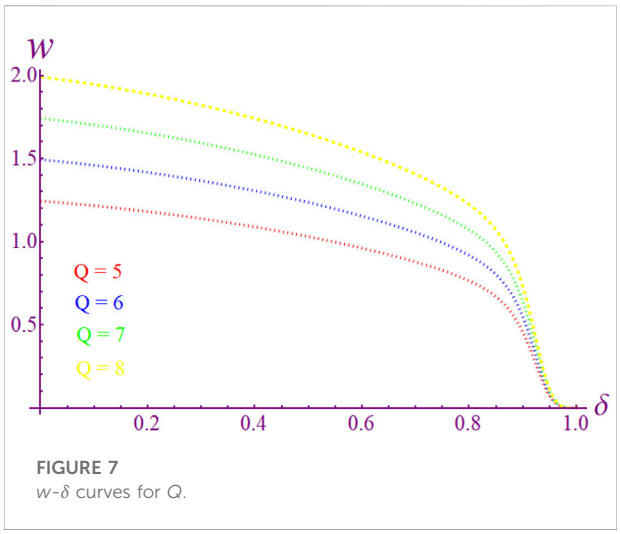

FIGURE 7
w-δ curves for *Q*.

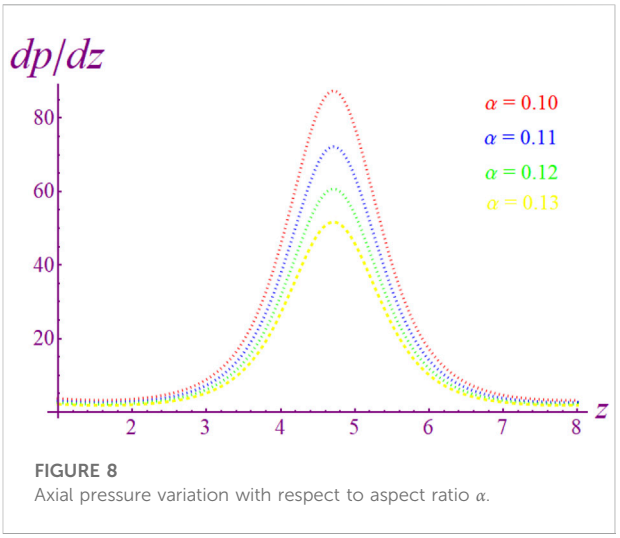

FIGURE 8
Axial pressure variation with respect to aspect ratio α.

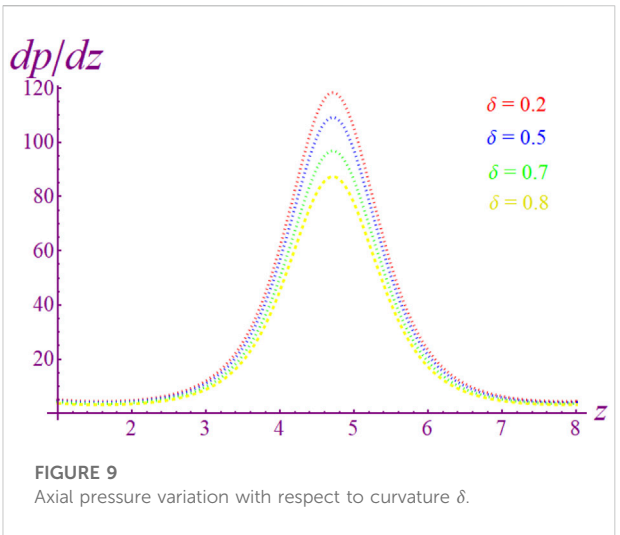

FIGURE 9
Axial pressure variation with respect to curvature δ.

mathematical sense, where larger waves with the same fixed height slow the flow because of the time required to relax the tissues and push the fluid forward compared to low-amplitude waves that allow faster release of the fluid over a short duration. Figure 4 shows that the flow rate is directly related to the flow speed, where a large flow rate suggests that the fluid particles travel more quickly for a larger rate of flow per unit area.

To investigate the velocity attributes for various curvature parameters, Figure 5 suggests the impact of α such that an increase in the section curvature in the range $0 < \delta < 0.5$ lowers fluid speed but remains fixed for various values of the aspect ratio; however, these results decrease in the range $0.5 < \delta < 1$. This shows that a small change in the curvature does not significantly affect the aspect ratio of the duct cross section but a larger curvature considerably affects the aspect ratio and flow speed. Figure 6 indicates that ϕ has inverse effects on the velocity curves in

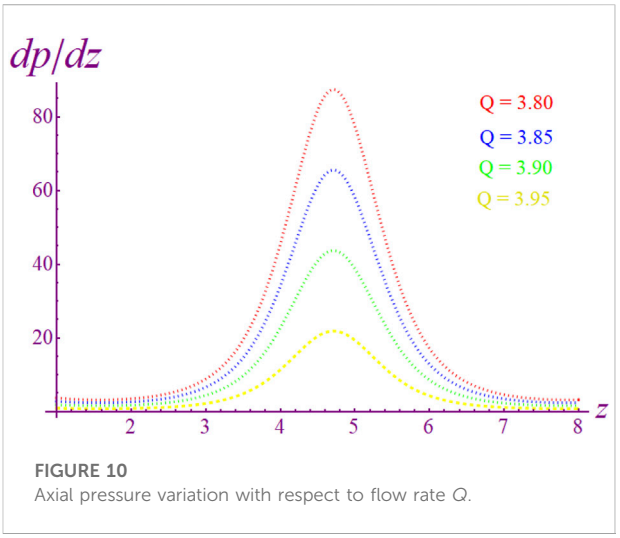

FIGURE 10
Axial pressure variation with respect to flow rate *Q*.

10.3389/fphy.2022.961201

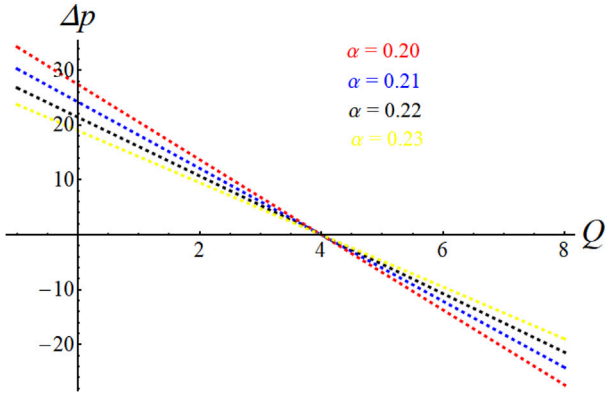

FIGURE 11
Pressure Δp variation with respect to aspect ratio α.

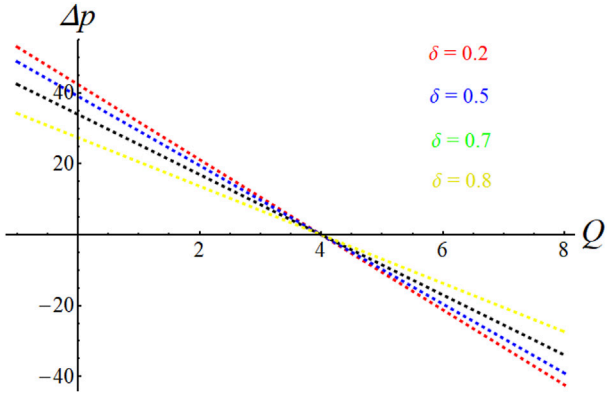

FIGURE 12
Pressure Δp variation with respect to curvature δ.

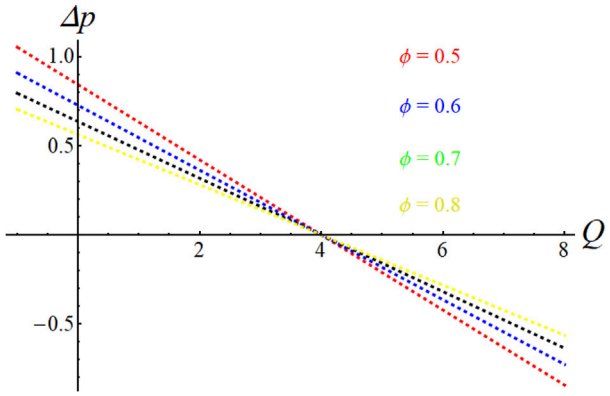

FIGURE 13
Pressure Δp variation with respect to amplitude ratio ϕ.

curved domains and that the curves show more significant variations in their heights than in the previous figure. In case of flow rate (Figure 7), the velocity increases with the flow rate. Physically, this indicates that when the flow per unit volume increases, the fluid molecules pass through more freely and gain more speed accordingly. It is also obvious from these three figures that the duct curvature affects the flow velocity inversely. It is also seen that the velocity is maximum for no curvature, i.e., $\delta = 0$, and is minimum for $\delta = 1$.

Figure 8 indicates that the pressure gradient dp/dz plotted against flow rate Q shows sinusoidal variation of the curves in accordance with the function for the sinusoidal waves at the boundaries. It is also noted here that the pressure decreases with increasing aspect ratio. Further, it is noted that the largest pressure gradient is observed at the center of the domain, which depicts that greater pressure is needed to conserve momentum in the flow. Figure 9 shows that the pressure decreases against the domain curvature and that the pressure gradient is quite large ($\approx$ 120 units) for the lowest value of $\delta = 0.2$, which was not true even with the lowest aspect ratio of $\alpha = 0.1$, as noted in the previous graph. Figure 10 suggests that the flow rate also produces smaller changes in the axial pressure; however, it is quite interesting that a larger flow rate enables a very low pressure of $\approx$ 20 units, which is the lowest value among these three diagrams.

To discuss peristaltic pumping, the graph of Δp against the flow rate Q is shown in Figure 11 for the effects of the aspect ratio α. It is noted that when we increase the aspect ratio of the conduit, the intersecting lines are reduced in height in the peristaltic pumping region $Q \in [0, 4]$, which depicts that a large aspect ratio produces a smaller increase in pressure in the positive pumping region; however in the fourth quadrant, increased negative or reverse pumping occurs, meaning that a large aspect ratio can result in greater intensity of reverse pumping. It can also be measured that co-pumping occurs at $Q = 4$. From Figures 12, 13, the readings are similar to those noted for Figure 11. In Figure 12, the decrease in pumping rate against curvature shows that if the curvature of the duct increases, the pumping rate diminishes considerably, which produces large-scale reverse pumping; the same argument holds for the amplitude ratio in Figure 13.

Figure 14 can be discussed under the stream bolus structure of the flow problem for α. Here, we see that a large value of α produces a forcing effect on the boluses, which then become smaller in size and are broken when we further increase the value; that is, a single bolus was surrounded by the four streamlines for $\alpha = 0.5$, two boluses were generated and surrounded by five streamlines for $\alpha = 0.6$, and a single bolus is again surrounded by three lines for $\alpha = 0.7$. These variations indicate that there are variable measurements for the trapped boluses for the aspect ratio. Figure 15 shows that when the duct is more curved by increasing the curvature, it produces a large number of small-sized boluses that are circulated by the increasing number of streamlines; further, it is observed that when the curvature of the duct increases, the fluid pressure increases and results in an increasing number of boluses. Table 1 validates the current data with findings from existing

10.3389/fphy.2022.961201

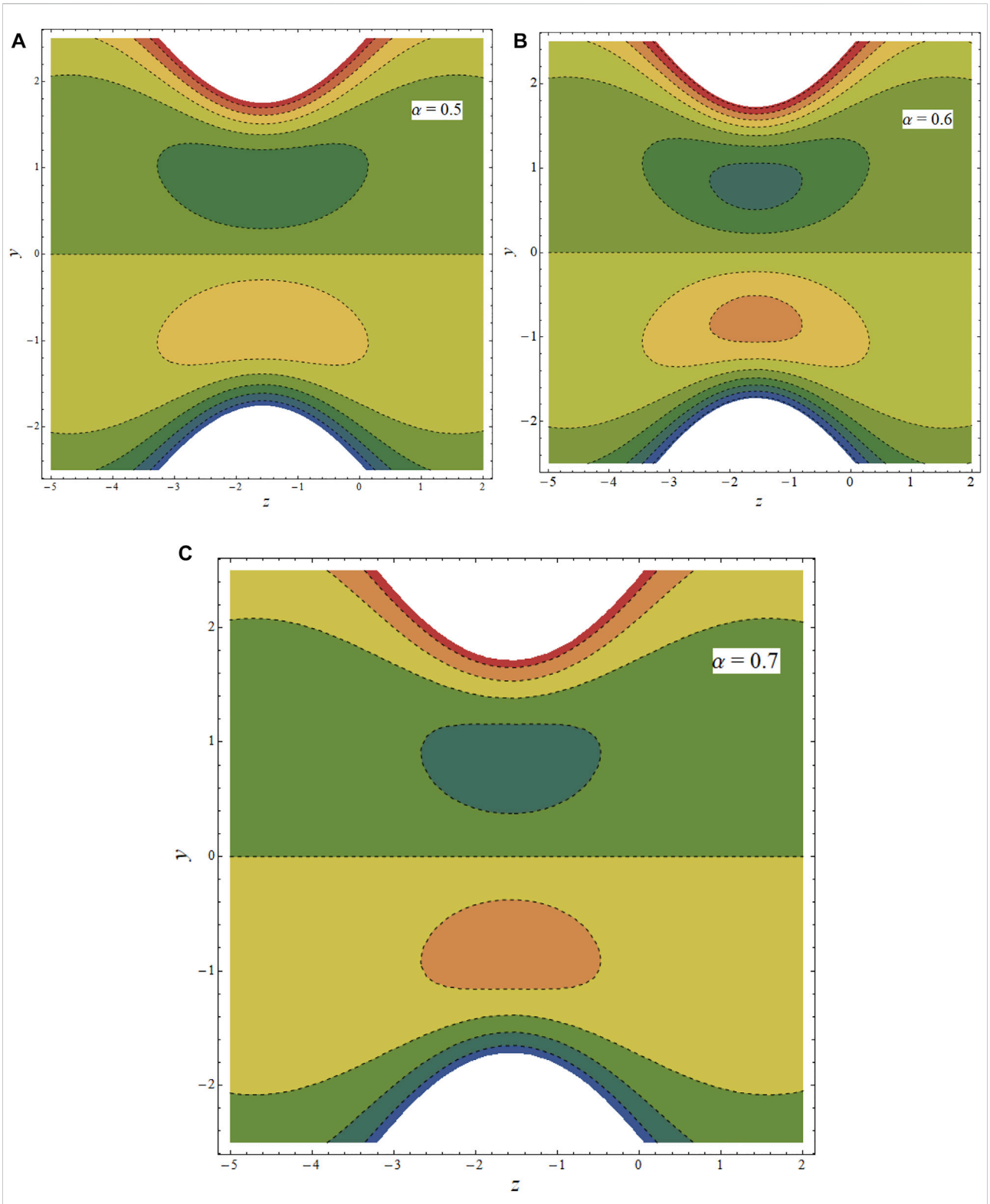

FIGURE 14
Trapped bolus scheme for α.

10.3389/fphy.2022.961201

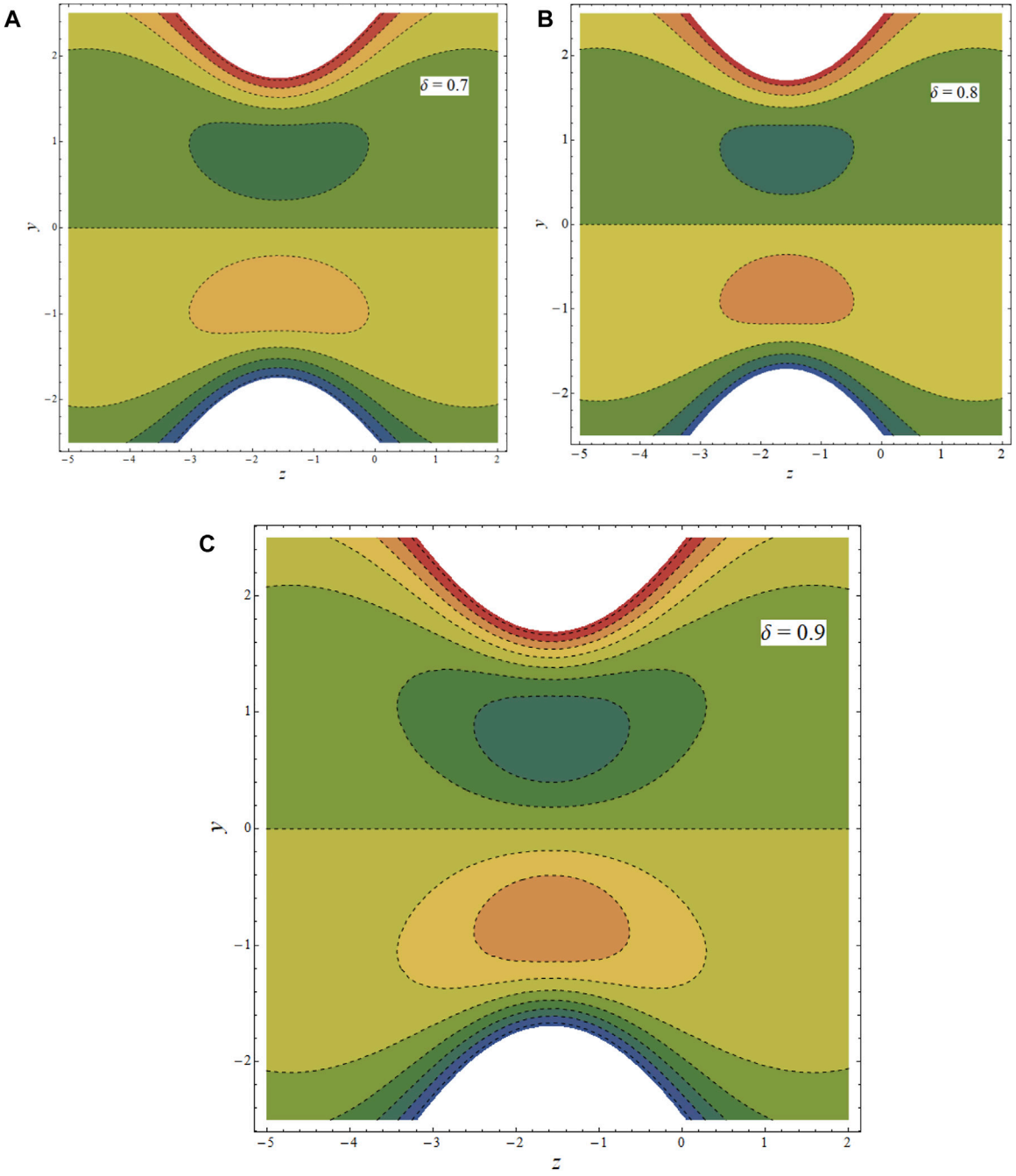

FIGURE 15
Trapped bolus scheme for δ.

TABLE 1 Comparison of curved and straight ducts [37].

Flow rate	Pressure increase in a straight duct [37]	Pressure increase in a duct with zero curvature	Pressure increase in a duct with nonzero curvature
−1	*7.80917*	*7.80916*	*4.69047*
−0.6	*4.6855*	*4.6853*	*2.81428*
−0.2	*1.56183*	*1.56178*	*0.938094*
0.2	*−1.56183*	*−1.56181*	*−0.938094*
0.6	*−4.6855*	*−4.6852*	*−2.81428*
1	*−7.80917*	*−7.80908*	*−4.69047*
1.4	*−10.9328*	*−10.9319*	*−6.56665*
1.8	*−14.0565*	*−14.0554*	*−8.44284*
2.2	*−17.1802*	*−17.1813*	*−10.319*
2.6	*−20.3038*	*−20.3021*	*−12.1952*
3	*−23.4275*	*−23.4265*	*−14.0714*

literature. It is easily noted that when the curvature values of the geometry are minimized, the results of present work are similar to those of the straight duct calculations [37]; moreover, for nonzero curvature, the pressure increase in the curved duct is smaller than that of the straight duct [37].

Conclusion

In the present work, we discussed the peristaltic flow scheme for a Newtonian fluid in an enclosed curved duct with a rectangular cross section for the first time. After incorporating the large wavelength and low Reynolds number approximations, the obtained PDE was examined analytically for the well-known HPM using the computational software Mathematica and the algorithm of the DSolve command. The pressure increase and stream functions are obtained using the NIntegrate and Integrate tools, respectively. The analytical solutions are discussed through graphs, whose observations have been elaborated in detail. The key results of the study are summarized as follows:

1) The velocity in a curved duct can be reduced by increasing the aspect ratio and amplitude ratio, but the flow rate shows opposite results. It is also noted that the velocity is a decreasing function of the curvature and is maximum for a smaller curvature.
2) It is observed that when the aspect ratio, curvature, and flow rate increase, the axial pressure slope declines.
3) It is also observed that the aspect ratio, curvature, and amplitude ratio have inverse impacts on peristaltic pumping compared to reverse pumping.
4) From the trapped bolus graphs, it is noted that the aspect ratio and duct curvature produce low numbers of smaller sized boluses, whereas the amplitude ratio produces a greater number of larger sized boluses.
5) The results of the current investigation are in agreement with those of existing literature [37] when considering the special case with zero curvature; further, the pressure increase is smaller in a curved duct than a straight one.

Data availability statement

The original contributions of this study are included in the article/supplementary material, and any further inquiries can be directed to the corresponding author.

Author contributions

All authors listed have made substantial, direct, and intellectual contributions to the work and approved it for publication.

Acknowledgments

The authors extend their appreciation to the Deanship of Scientific Research at King Khalid University for funding this work through Large Groups. [Project under grant number (RGP.2/116/43)].

Conflict of interest

The authors declare that this research was conducted in the absence of any commercial or financial relationships that could be construed as potential conflicts of interest.

Publisher's note

References

1. Shapiro AH, Jaffrin MY, Weinberg SL. Peristaltic pumping with long wavelengths at low Reynolds number. *J Fluid Mech* (1969) 37(4):799–825. doi:10.1017/s0022112069000899

2. Ramana Kumari AV, Radhakrishnamacharya G. Effect of slip and magnetic field on peristaltic flow in an inclined channel with wall effects. *Int J Biomath* (2012) 5(06):1250015. doi:10.1142/s1793524511001568

3. Mekheimer KS. Peristaltic flow of blood under effect of a magnetic field in a non-uniform channels. *Appl Maths Comput* (2004) 153(3):763–77. doi:10.1016/s0096-3003(03)00672-6

4. Rashid M, Ansar K, Nadeem S. Effects of induced magnetic field for peristaltic flow of Williamson fluid in a curved channel. *Physica A: Stat Mech its Appl* (2020) 553:123979. doi:10.1016/j.physa.2019.123979

5. Haroun MH. Non-linear peristaltic flow of a fourth grade fluid in an inclined asymmetric channel. *Comput Mater Sci* (2007) 39(2):324–33. doi:10.1016/j.commatsci.2006.06.012

6. Javed M, Naz R. Peristaltic flow of a realistic fluid in a compliant channel. *Physica A: Stat Mech its Appl* (2020) 551:123895. doi:10.1016/j.physa.2019.123895

7. Akram S, Athar M, Saeed K. Hybrid impact of thermal and concentration convection on peristaltic pumping of Prandtl nanofluids in non-uniform inclined channel and magnetic field. *Case Stud Therm Eng* (2021) 25:100965. doi:10.1016/j.csite.2021.100965

8. Krishna MV, Reddy MG, Chamkha AJ. Heat and mass transfer on MHD free convective flow over an infinite nonconducting vertical flat porous plate. *Inter J Fluid Mech Res* (2019) 46(1)–25. doi:10.1615/interjfluidmechres.2018025004

9. Khan LA, Raza M, Mir NA, Ellahi R. Effects of different shapes of nanoparticles on peristaltic flow of MHD nanofluids filled in an asymmetric channel. *J Therm Anal Calorim* (2020) 140(3):879–90. doi:10.1007/s10973-019-08348-9

10. Krishna MV, Chamkha AJ. Hall and ion slip effects on MHD rotating flow of elastico-viscous fluid through porous medium. *Int Commun Heat Mass Transfer* (2020) 113:104494. doi:10.1016/j.icheatmasstransfer.2020.104494

11. Akram J, Akbar NS, Tripathi D. Analysis of electroosmotic flow of silver-water nanofluid regulated by peristalsis using two different approaches for nanofluid. *J Comput Sci* (2022) 62:101696. doi:10.1016/j.jocs.2022.101696

12. Krishna MV, Reddy MG, Chamkha AJ. Heat and mass transfer on unsteady MHD flow through an infinite oscillating vertical porous surface. *J Porous Media* (2021) 24(1):81–100. doi:10.1615/jpormedia.2020025021

13. Akram S, Razia A, Afzal F. Effects of velocity second slip model and induced magnetic field on peristaltic transport of non-Newtonian fluid in the presence of double-diffusivity convection in nanofluids. *Arch Appl Mech* (2020) 90(7):1583–603. doi:10.1007/s00419-020-01685-4

14. Akbar NS, Maraj EN, Noor NFM, Habib MB. Exact solutions of an unsteady thermal conductive pressure driven peristaltic transport with temperature-dependent nanofluid viscosity. *Case Stud Therm Eng* (2022) 35:102124. doi:10.1016/j.csite.2022.102124

15. Sewify GH, Javid K, Adeel M, Abbasi A, Khan SU, Omri M, et al. Blood flow in multi-sinusoidal curved passages with biomimetic rheology: An application of blood pumping. *Mathematics* (2022) 10(9):1579. doi:10.3390/math10091579

16. Akram J, Akbar NS, Tripathi D. Entropy generation in electroosmotically aided peristaltic pumping of MoS2 Rabinowitsch nanofluid. *Fluid Dyn Res* (2022) 54(1):015507. doi:10.1088/1873-7005/ac4e7b

17. Javid K, Kolsi L, Al-Khaled K, Omri M, Khan SU, Abbasi A. Biomimetic propulsion of viscoelastic nanoparticles in a curved pump with curvature and slip effects: Blood control bio-medical applications. In: *Waves in random and complex media* (2022). p. 1–18.

18. Hina S, Hayat T, Alsaedi A. Heat and mass transfer effects on the peristaltic flow of Johnson–Segalman fluid in a curved channel with compliant walls. *Int J Heat Mass Transfer* (2012) 55(13-14):3511–21. doi:10.1016/j.ijheatmasstransfer.2012.03.014

19. Nadeem S, Shahzadi I. Mathematical analysis for peristaltic flow of two phase nanofluid in a curved channel. *Commun Theor Phys* (2015) 64(5):547–54. doi:10.1088/0253-6102/64/5/547

20. Kalantari A, Sadeghy K, Sadeqi S. Peristaltic flow of non-Newtonian fluids through curved channels: A numerical study. *a a* (2013) 100:2.

21. Tanveer A, Hayat T, Alsaadi F, Alsaedi A. Mixed convection peristaltic flow of Eyring-Powell nanofluid in a curved channel with compliant walls. *Comput Biol Med* (2017) 82:71–9. doi:10.1016/j.compbiomed.2017.01.015

22. Nadeem S, Maraj EN. The mathematical analysis for peristaltic flow of hyperbolic tangent fluid in a curved channel. *Commun Theor Phys* (2013) 59(6):729–36. doi:10.1088/0253-6102/59/6/14

23. Xiong PY, Javid K, Raza M, Khan SU, Khan MI, Chu YM. MHD flow study of viscous fluid through a complex wavy curved surface due to bio-mimetic propulsion under porosity and second-order slip effects. *Commun Theor Phys* (2021) 73(8):085001. doi:10.1088/1572-9494/abfcb2

24. Javed M, Imran N, Rao AI. Design and testing of varying magnetic field effect in a pulsatility blood flow of viscoelastic material: Flexibility analysis in a curved channel. *Heat Transfer* (2021) 50(6):6358–76. doi:10.1002/htj.22175

25. Nadeem S, Sadaf H. Theoretical analysis of Cu-blood nanofluid for metachronal wave of cilia motion in a curved channel. *IEEE Trans Nanobioscience* (2015) 14(4):447–54. doi:10.1109/tnb.2015.2401972

26. Nadeem S, Sadaf H. Ciliary motion phenomenon of viscous nanofluid in a curved channel with wall properties. *Eur Phys J Plus* (2016) 131(3):65–10. doi:10.1140/epjp/i2016-16065-y

27. Arooj A, Javed M, Imran N, Sohail M, Yao SW. Pharmacological and engineering biomedical applications of peristaltically induced flow in a curved channel. *Alexandria Eng J* (2021) 60(6):4995–5008. doi:10.1016/j.aej.2021.04.010

28. Nadeem S, Sadaf H. Exploration of single wall carbon nanotubes for the peristaltic motion in a curved channel with variable viscosity. *J Braz Soc Mech Sci Eng* (2017) 39(1):117–25. doi:10.1007/s40430-016-0612-9

29. Reddy MS, Mishra M, Sreenadh S, Rao AR. Influence of lateral walls on peristaltic flow in a rectangular duct. *J Fluids Eng* (2005) 127:824–7. doi:10.1115/1.1994876

30. Nadeem S, Akram S. Peristaltic flow of a Jeffrey fluid in a rectangular duct. *Nonlinear Anal Real World Appl* (2010) 11(5):4238–47. doi:10.1016/j.nonrwa.2010.05.010

31. Riaz A. Thermal analysis of an Eyring–Powell fluid peristaltic transport in a rectangular duct with mass transfer. *J Therm Anal Calorim* (2021) 143(3):2329–41. doi:10.1007/s10973-020-09723-7

32. Abbas MA, Bai YQ, Bhatti MM, Rashidi MM. Three dimensional peristaltic flow of hyperbolic tangent fluid in non-uniform channel having flexible walls. *Alexandria Eng J* (2016) 55(1):653–62. doi:10.1016/j.aej.2015.10.012

33. Dolon SN, Hasan MS, Lorenzini G, Mondal RN. A computational modeling on transient heat and fluid flow through a curved duct of large aspect ratio with centrifugal instability. *Eur Phys J Plus* (2021) 136(4):382–27. doi:10.1140/epjp/s13360-021-01331-0

34. Biazar J, Ghazvini H. Convergence of the homotopy perturbation method for partial differential equations. *Nonlinear Anal Real World Appl* (2009) 10(5):2633–40. doi:10.1016/j.nonrwa.2008.07.002

35. Mohyud-Din ST, Noor MA. Homotopy perturbation method for solving partial differential equations. *Z für Naturforschung A* (2009) 64(3-4):157–70. doi:10.1515/zna-2009-3-402

36. Biazar J, Eslami M. A new homotopy perturbation method for solving systems of partial differential equations. *Comput Maths Appl* (2011) 62(1):225–34. doi:10.1016/j.camwa.2011.04.070

37. Riaz A, Nadeem S, Ellahi R, Zeeshan A. Exact solution for peristaltic flow of Jeffrey fluid model in a three dimensional rectangular duct having slip at the walls. *Appl Bionics Biomech* (2014) 11(1-2):81–90. doi:10.1155/2014/901313

Nomenclature

Symbols

h height [m]

d width [m]

$\boldsymbol{c}$ wave speed [m/s]

$\bar{F}$ flow rate [m^3/s]

t time coordinate [s]

(u, v, w) velocity components [m/s]dimensionless velocity components

ρ density [kg/m^3]

μ viscosity [Ns/m^2]

$\tilde{a}$ wall function [m]

b amplitude [m]

λ wavelength [m]

L length [m]

p pressure [Pa]

Dimensionless symbols

$\bar{t}$, $\bar{x}$, $\bar{y}$, $\bar{z}$ dimensionless coordinates

(r, θ, y) cylindrical coordinates

(x, y, z) transformed coordinates

D derivative operator

$\bar{p}$ dimensionless pressure

(u, v, w) velocity components [m/s]dimensionless velocity components

$\bar{a}$ dimensionless wall function

ξ dimensionless wavenumber

α aspect ratio

δ dimensionless curvature

Re Reynolds number

ϕ amplitude ratio

Q dimensionless flow rate